Upper-Ocean Heat Balance in the Kuroshio Extension Region*

BO QIU AND KATHRYN A. KELLY

Department of Physical Oceanography, Woods Hole Oceanographic Institution, Woods Hole, Massachusetts

(Manuscript received 1 October 1992, in final form 8 March 1993)

ABSTRACT

A horizontally two-dimensional mixed-layer model is used to study the upper-ocean heat balance in the Kuroshio Extension region (30°–40°N, 141°–175°E). Horizontal dependency is emphasized because, in addition to vertical entrainment and surface thermal forcing, horizontal advection and eddy diffusion make substantial contributions to changes in the upper-ocean thermal structure in this region. By forcing the model using the wind and heat flux data from ECMWF and the absolute sea surface height data deduced from the Geosat ERM, the mixed-layer depth (h_m) and temperature (T_m) changes in the Kuroshio Extension are hindcast for a 2.5-year period (November 1986–April 1989). Both phase and amplitude of the modeled T_m and h_m variations agreed well with the climatology. The horizontal thermal patterns also agreed favorably with the available in situ SST observations, but this agreement depended crucially on the inclusion of horizontal advections.

Although the annually averaged net heat flux from the atmosphere to the ocean (Q_{net}) is negative over the Kuroshio Extension region, the effect of the surface thermal forcing, when integrated annually, is to increase T_m because the large, negative Q_{net} in winter is redistributed in a much deeper mixed layer than it is in summer when $Q_{net} > 0$. This warming effect is counterbalanced by the vertical turbulent entrainment through the base of the mixed layer (35% when annually integrated), the Ekman divergence (16%), the geostrophic divergence (12%), and the horizontal eddy diffusion (35%). Though small when averaged in space and time, the temperature advection by the surface flows makes a substantial contribution to the local heat balances. While it warms the upstream region of the Kuroshio Extension (west of 150°E), the current advection tends to cool the upper ocean over the vast downstream region due to the presence of the recirculation gyre.

1. Introduction

A knowledge of the heat and momentum exchange across the air–sea interface is crucial to our understanding of global climate change and the coupling between atmosphere and ocean. The heat exchange in particular depends on physical variables such as sea surface temperature (SST) and heat content of the upper ocean. Previous studies by Isemer and Hasse (1987), Hsiung (1985), and Talley (1984) among others showed that the ocean, when averaged annually, loses a significant portion of heat to the atmosphere in regions where western boundary currents, such as the Gulf Stream and the Kuroshio, separate from the coasts. Although such a heat loss per se is not surprising, considering the tremendous heat fluxes carried northward by these currents from low latitudes, the roles the boundary currents play in determining the upper-ocean thermal structure and in influencing the adjacent ocean circulation are not well understood.

A useful approach to studying the upper ocean has been to focus on the physics of the relatively well-mixed surface layer (the mixed layer). Kraus and Turner's (1967) pioneering work formulated the turbulent kinetic energy balance in the mixed layer and related the vertical turbulent mixing to atmospheric wind and buoyancy forcing. Since then many studies have contributed to the modification and further development of mixed-layer dynamics by including, for example, shortwave radiation penetration, effect of salt flux, and parameterizations of shear effects across the mixed-layer interface (Denman 1973; Niiler 1975; Niiler and Kraus 1977; Garwood 1977; Davis et al. 1981). Using one-dimensional upper-ocean models, several investigators have further compared the mixed-layer theory with in situ ocean observations and have achieved reasonable success in simulating fluctuations of the upper-ocean thermal structures on a time scale longer than a few days (e.g., Denman and Miyake 1973; Thompson 1976; Davis et al. 1981; Martin 1985). For fluctuations shorter than this time scale, however, Price et al. (1986) showed that it is necessary to fully resolve the vertical shear (or the Froude number dependency) of the upper ocean.

In most of the past studies, emphasis has been placed on one-dimensional models that neglect the influence of advection due to Ekman and geostrophic flows. Although the importance of the horizontal advection in

* Woods Hole Oceanographic Institution Contribution Number 8253.

Corresponding author address: Dr. Bo Qiu, Department of Physical Oceanography, Woods Hole Oceanographic Institution, Woods Hole, MA 02543.

the upper-ocean heat budget was recognized, lack of contemporaneous surface velocity observations has limited those studies either to focusing on the advection due to the Ekman transport alone (Paduan and de Szoeke 1986), or to using climatology to evaluate the surface geostrophic flows (McPhaden 1982; Stevenson and Niiler 1983; Bryden and Brady 1985; Enfield 1986). In the western boundary current extension region, we expect that both the Ekman and geostrophic flows and their fluctuations will make substantial contributions to the upper-ocean thermal structures.

With the completion of the U.S. Navy's Geosat Exact Repeat Mission (ERM) for a three-year period from November 1986 to November 1989, the altimetrically measured sea surface height data provided us a new means to estimate the surface geostrophic velocity field. For the boundary current extension regions, the altimetric data can be particularly useful because of the large signal/noise ratio. One problem in extracting the surface velocities from the altimetric measurement is that the mean surface height information is lost in order to remove the unknown earth's geoid. This limits the altimetric measurement to providing only the residual component of the surface height (i.e., the height deviations from the temporal mean). To overcome this shortcoming, Kelly and Gille (1990) recently developed a simple kinematic model that allows one to recover the mean surface height profile of a boundary current using the residual height data. The kinematic model exploits the distinct slope characteristics between the mean and the instantaneous height profiles of the boundary current and reconstructs the mean height profile along a satellite subtrack through successive fitting of the observed and modeled height profiles. This model was recently further extended by Qiu et al. (1991) to estimate the mean surface height field in a two-dimensional space through an inverse approach that combines the ascending and descending subtrack data. Applying the method to the Kuroshio Extension region, Qiu et al. showed that the estimated mean surface height field (Fig. 1) agrees well with the surface dynamic height derived from the climatological hydrographic data. Based on this mean surface height field and using an objective analysis method, they obtained the absolute surface height field of the Kuroshio Extension for the first 2.5 years of the Geosat ERM and discussed the energetics, eddy propagation, and annual/interannual fluctuations in the Kuroshio Extension.

In the present study, this surface height dataset is used to infer the surface geostrophic flows of the Kuroshio Extension. Using a horizontally two-dimensional upper-ocean model that hindcasts the mixed-layer temperature and depth, we seek to clarify the roles played by the current advection in determining the upper-ocean heat balance. Notice that both horizontal and vertical heat advection can be important to the ocean circulation adjacent to the boundary current extensions. For example, the heat flux transferred southward is influential in the intensity of the recirculation gyres (e.g., Masuzawa 1972; Worthington 1976), and the vertical heat transfer through the base of the mixed layer is an important quantity for the formation of the subtropical mode waters (e.g., Talley and Raymer 1982; Hanawa 1987; Bingham 1992). Understanding the upper-ocean heat balance, thus, can also shed light on the ocean circulation variability adjacent to the Kuroshio Extension.

In the next section, an upper-ocean model including horizontal advection and eddy fluxes is formulated. Section 3 describes the model implementation and the observational data used in the model calculations. In

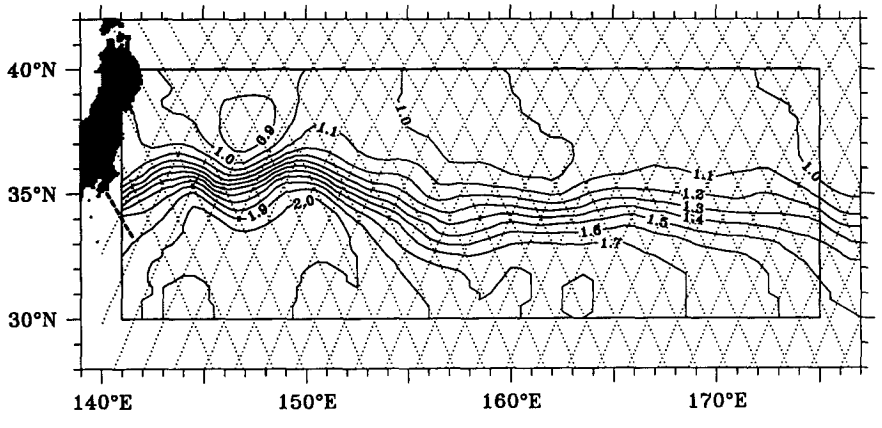

FIG. 1. Mean sea surface height field in the Kuroshio Extension derived from the 2.5-year Geosat altimetry data. Units for the height contours are meters. Thin dotted lines denote ascending and descending tracks of the Geosat that are used in mapping the absolute surface height field (see Qiu et al. 1991). The solid square denotes the model basin for numerical calculations and the dashed line across the inflow Kuroshio indicates the repeat section of CTD and XBT observations.

section 4, the model performance is discussed through comparisons with available in situ observations and climatological data. The role of the Kuroshio Extension is considered in section 5, and section 6 summarizes the results from the present study.

2. Formulation of the model

Temperature variations in the upper ocean where horizontal velocities exist can be expressed by

$$\frac{\partial T}{\partial t} + \mathbf{u}\cdot\nabla T + w\frac{\partial T}{\partial z} - A_h\nabla^2 T + \frac{\partial}{\partial z}\overline{w'T'} = \frac{1}{\rho_0 c}\frac{\partial q}{\partial z}, \tag{1}$$

where $\mathbf{u} \equiv (u, v)$ are the horizontal velocity components, w is the vertical velocity component, A_h is the horizontal eddy diffusivity, $\nabla = (\partial/\partial x, \partial/\partial y)$ is the horizontal gradient operator, and $\partial\overline{w'T'}/\partial z$ is the vertical divergence of the turbulent heat flux. The rhs of Eq. (1) represents the local heat source due to the absorption of the shortwave radiation, wherein ρ_0 and c are the reference density and specific heat of seawater, q is the downward radiative flux given by

$$q(z) = q(0)[R\exp(z/\gamma_1) + (1-R)\exp(z/\gamma_2)], \tag{2}$$

where $q(0)$ is the shortwave radiative flux at the sea surface, R is a separation constant, and γ_1 and γ_2 are the attenuation length scales (see Paulson and Simpson 1977).

Many previous studies have considered the upper-ocean mixed-layer dynamics (see Introduction); without going into the details, we will briefly derive the model equations below with emphasis on the horizontal advection and subgrid-scale eddy fluxes. First, we define the mixed-layer depth to be the upper-ocean layer whose depth-averaged temperature is 1°C higher than the water temperature just below (T_d), namely,

$$\Delta T = T_m - T_d \equiv \frac{1}{h_m}\int_{-h_m}^{0} T(z)dz - T_d = 1°\text{C} \tag{3}$$

(hereafter, subscripts m and d denote quantities in and immediately below the mixed layer, respectively). A similar definition for the mixed-layer depth has been used by Lamb (1984) for the Atlantic Ocean. Assuming the mixed layer is bounded below by a thin entrainment boundary layer (which has a thickness $\delta \ll h_m$) and integrating Eq. (1) from $z = -h_m - \delta$ to the sea surface, we obtain the following equation governing the mixed-layer temperature T_m:

$$h_m\frac{\partial T_m}{\partial t} + \mathbf{U}_m\cdot\nabla T_m - A_h h_m\nabla^2 T_m + \overline{w'T'}(0) + \Delta T\left(\frac{\partial h_m}{\partial t} + \nabla\cdot\mathbf{U}_m\right) = \frac{1}{\rho_0 c}[q(0) - q(-h_m)]. \tag{4}$$

In deriving (4), we have neglected terms of order of δ and used the fact that the vertical turbulent mixing is negligible below the entrainment boundary layer and that the fluid velocity normal to the mixed-layer interface is continuous, namely, $w_d + \mathbf{u}_d\cdot\nabla h = w_m + \mathbf{u}_m\cdot\nabla h$ (deRuijter 1983). In Eq. (4), $\overline{w'T'}(0)$ represents the turbulent heat flux at the ocean surface, which is equal to the heat transfer due to longwave radiation and sensible and latent heat fluxes. In the following, a more convenient quantity, $Q_{\text{net}} \equiv q(0) - \rho_0 c\overline{w'T'}(0)$ (the net heat flux from the atmosphere to the ocean), will be used in place of $\overline{w'T'}(0)$. In Eq. (4), $\mathbf{U}_m \equiv \int_{-h_m}^{0}\mathbf{u}_m dz$ is the horizontal mass transport vector due to geostrophic and Ekman flows in the mixed layer:

$$V_m = -\frac{1}{f}\left(-gh_m\frac{\partial\eta}{\partial x} + \frac{\alpha g h_m^2}{2}\frac{\partial T_m}{\partial x} + \frac{\tau^x}{\rho_0}\right)$$

$$U_m = \frac{1}{f}\left(-gh_m\frac{\partial\eta}{\partial y} + \frac{\alpha g h_m^2}{2}\frac{\partial T_m}{\partial y} + \frac{\tau^y}{\rho_0}\right), \tag{5}$$

where f is the Coriolis parameter, η is the sea surface height, α is the thermal expansion coefficient ($= 2.5\times 10^{-4}$ °C^{-1}), and (τ^x, τ^y) are the (x, y) components of the wind stress. The second term on the rhs of (5) expresses the current shear effect associated with the horizontal temperature gradient in the mixed layer.

To close the model dynamics, an energy equation is necessary; it can be derived by multiplying Eq. (1) by $\alpha g(z - z_0)$ and by integrating it from $z = -h_m - \delta$ to $z = 0$, where z_0 is the reference level for the potential energy (see Davis et al. 1981). When including horizontal advection and eddy diffusion, the energy equation, after again neglecting the vertical turbulent flux below the entrainment layer and the terms of δ order and setting $z_0 = -h_m/2$, becomes

$$\frac{1}{2}\alpha g h_m\Delta T\left(\frac{\partial h_m}{\partial t} + \nabla\cdot\mathbf{U}_m - A_h\nabla^2 h_m\right) + \alpha g\int_{-h_m}^{0}\overline{w'T'}dz = -\frac{\alpha g h_m}{2\rho_0 c}[Q_{\text{net}} + q(-h_m)] + \frac{\alpha g}{\rho_0 c}\int_{-h_m}^{0} q(z)dz. \tag{6}$$

Notice that the buoyancy flux term $\alpha g\int_{-h_m}^{0}\overline{w'T'}dz$ gives the conversion rate between the turbulent kinetic energy (TKE) and potential energy. Based on the TKE budget, Davis et al. (1981) showed that this term can be parameterized by

$$-\alpha g\int_{-h_m}^{0}\overline{w'T'}dz = m_0 u_*^3 + m_s S - m_c\frac{\alpha g h_m}{4\rho_0 c}(|Q_{\text{net}}| - Q_{\text{net}}). \tag{7}$$

In Eq. (7), the first two terms on the rhs denote the energy sources of wind stirring (where $u_* \equiv (|\tau|/$

$\rho_0)^{1/2}$ is the frictional velocity) and shear production ($S \equiv -\int_{-h_m}^{0} \rho \overline{u'w'} \cdot \partial_z \mathbf{u} dz$). The third term denotes the energy dissipation under cooling conditions. Because S is not available from observations, we are unable to estimate the shear production term. For $m_s = 0$, the measurements of Davis et al. suggested that the appropriate value of m_0 is between 0.4 and 0.5. In the following calculations, we take $m_0 = 0.5$; effects of choosing different m_0 values will be discussed in section 6. The convective efficiency coefficient m_c is taken to be 0.83, which was determined by Deardorff et al. (1969) from laboratory experiments.

To relate the preceding equations to the one-dimensional mixed-layer theory, it is helpful to introduce the entrainment velocity w_e and rewrite the equations as follows:

$$\frac{\partial h_m}{\partial t} + \nabla \cdot \mathbf{U}_m = A_h \nabla^2 h_m + w_e, \tag{8}$$

$$h_m \frac{\partial T_m}{\partial t} + \mathbf{U}_m \cdot \nabla T_m = A_h h_m \nabla^2 T_m + \frac{1}{\rho_0 c}(Q_{\text{net}} - q_d) - \Delta T(w_e + A_h \nabla^2 h_m), \tag{9}$$

$$\frac{1}{2} \alpha g h_m \Delta T w_e = m_0 u_*^3 + \frac{\alpha g}{\rho_0 c} \int_{-h_m}^{0} q(z) dz - \frac{\alpha g h_m}{2\rho_0 c}(Q_{\text{net}} + q_d) - m_c \frac{\alpha g h_m}{4\rho_0 c}(|Q_{\text{net}}| - Q_{\text{net}}). \tag{10}$$

When the surface meteorological and sea surface height data are prescribed, Eqs. (8)–(10) form a closed dynamic system for T_m and h_m. Notice that when the mixed layer is in the shoaling phase, $w_e = 0$, and the mixed-layer depth change due to the vertical turbulent mixing is such that h_m detrains instantly to the Monin–Obukhov depth:

$$h_m = \left[m_0 u_*^3 + \frac{\alpha g}{\rho_0 c} \int_{-h_m}^{0} q(z) dz \right] \Big/ \frac{\alpha g}{2\rho_0 c}(Q_{\text{net}} + q_d) \tag{11}$$

(cf. Kraus and Turner 1967). This depth is a result of Eq. (10), expressing the TKE balance between the effects of wind stirring and stabilization due to surface warming.

3. Model input and implementation

The upper-ocean model detailed in the previous section is applied to the Kuroshio Extension to study the upper-ocean heat balance in this typical western boundary current extension region. The model covers the area from 30° to 40°N and from 141° to 175°E (see Fig. 1). In this section, we describe the meteorological and sea surface height data used in the model calculations. This is followed by descriptions of the implementation of the numerical model, including specification of the model's initial and boundary conditions.

a. Sea surface height field

The sea surface height data derived from the first 2.5-year Geosat ERM (15 November 1986–30 April 1989) are used in this study to infer the geostrophic flows in the surface Kuroshio Extension. The details of determining the absolute surface height (i.e., the mean plus the residual component) from the Geosat altimetric measurements are expounded in Qiu et al. (1991). Here, we will simply point out that the mean surface height field, which is not readily available from the altimetric measurements, was determined by first estimating the mean surface height profiles along ascending and descending subtracks using the kinematic method of Kelly and Gille (1990) and then by combining these profiles through a least-squares fitting. This mean surface height was then added to the objectively mapped residual height data and interpolated to the model grid with a one-day time interval. For the objective mapping, we used the covariance function of the form:

$$\exp\left[-\left(\frac{2\Delta x}{R_x}\right)^2 - \left(\frac{2\Delta y}{R_y}\right)^2 - \left(\frac{2\Delta t}{R_t}\right)^2 \right], \tag{12}$$

where Δx, Δy, and Δt are distances from grid points to observation points in the x, y, and t axes and the influence radii $R_x = 145$ km, $R_y = 83$ km, and $R_t = 30$ days were determined from the original residual height data of Geosat.

b. Surface wind-stress field

The surface wind data, necessary to compute the Ekman transport as well as the surface wind stirring effect, are the twice-daily 1000-mb wind vectors analyzed by the European Centre for Medium-Range Weather Forecasts (ECMWF) and are provided to us from the National Center for Atmospheric Research (NCAR). The wind vectors, at a horizontal resolution of 2.5° × 2.5°, are first converted to the surface wind stress vectors using the bulk aerodynamic formulas proposed by Trenberth et al. (1990). To ensure that the geostrophic transport determined from the altimetric data and the Ekman transport from the wind-stress data in Eq. (5) have similar temporal scales, we low-pass filtered the wind-stress data by using the same Gaussian filter, $\exp[-(2\Delta t/R_t)^2]$, given in (12). The low-pass filtered wind-stress data were then interpolated linearly to the model grid and subsampled daily. Figure 2 shows the time series of the wind stress amplitude $|\tau|$ averaged in the model basin and its spatial pattern averaged in 1987 and 1988.

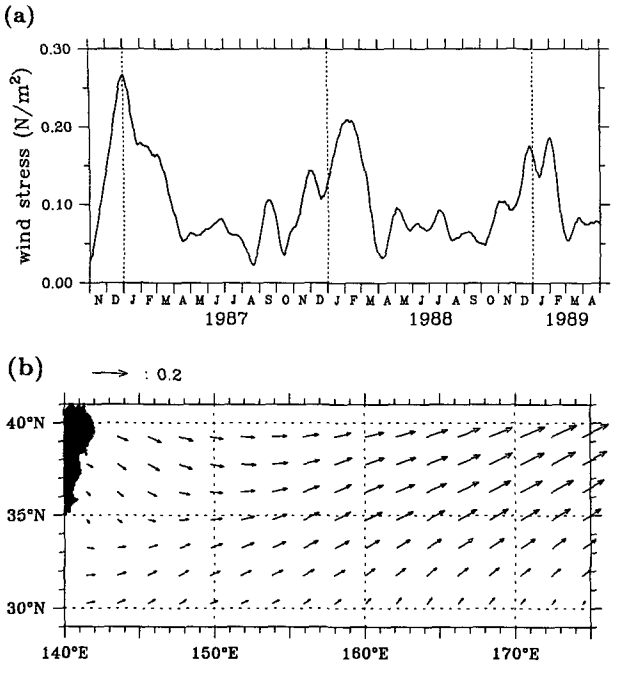

FIG. 2. (a) Time series of the low-pass filtered ECMWF surface wind-stress magnitude averaged in the model basin for the period of the Geosat ERM. (b) Horizontal pattern of the ECMWF surface wind stress averaged in 1987 and 1988 (units in N m^{-2}).

c. *Surface heat flux field*

Like the wind data, we used the surface heat flux data, namely, the shortwave radiation, the longwave radiation, the sensible heat, and the latent heat data from ECMWF (see Barnier and Simonot 1990). The heat flux data, also provided by NCAR, are 6-h accumulated values sampled at 0600–1200 UTC and 1800–2400 UTC and have a horizontal resolution of 1.125° × 1.125°. While the twice-daily flux data of the longwave radiation, sensible heat, and latent heat can be readily averaged to form the daily means, the shortwave radiation value $q(0)$ has to be treated specially due to its strong diurnal dependence. To obtain the daily mean $q(0)$ from the 6-h accumulated ECMWF data, we used the following procedures.

Theoretically, the shortwave solar radiation can be computed using estimates of clear-sky radiation and a correction factor for cloud cover:

$$q(0) = [A \sin\alpha a^{csc\alpha} + \frac{1}{2} A \sin\alpha(0.91 - a^{csc\alpha})]C \quad (13)$$

(see List 1984), where $\sin\alpha = \cos\theta \cos\phi \cos\xi + \sin\theta \sin\phi$, A is the solar constant (=1395 W m^{-2}), ϕ is the latitude of the model grid, θ is the declination of the sun, ξ is the hour angle of the sun, a is the atmospheric transmission coefficient (=0.7), and C is the cloud coverage in %. Using Eq. (13), we computed the clear-sky radiation values and inferred the cloud cover C by comparing them with the two 6-h accumulated $q(0)$ data from ECMWF. Using the C value averaged from the two estimates, the daily mean shortwave radiation was calculated by integrating Eq. (13). After obtaining the daily mean values of the four heat flux components, we again low-pass filtered them to remove fluctuations with time scales shorter than a few weeks. Figure 3a shows the time series of $q(0)$ and Q_{net} (the sum of the four components) averaged in the model basin for the 2.5-year Geosat period. The spatial pattern of the Q_{net} averaged in 1987 and 1988 is shown in Fig. 3b; both the pattern and the magnitude agree well with the former estimation by Hsiung (1985). In computing the downward radiative flux of Eq. (2), we used $R = 0.77$, $\gamma_1 = 1.5$ m, and $\gamma_2 = 14$ m, which correspond to Type II surface water in the classification of Jerlov (1968).

d. *Implementation of the numerical model*

Given the daily sea surface height, wind stress, and heat flux data, the mixed-layer temperature and depth in the model basin are solved numerically on a staggered grid system according to Eqs. (8)–(11). The grid spacing is 1° in longitude and 0.5° in latitude. These scales are determined primarily by the resolution of the observations. In the numerical calculation, η is defined on the corners of a grid box, U_m and V_m on the lateral sides, and all other variables at the center of the grid box. The time stepping is 1/4 day, which is constrained by the CFL condition in the advective Ku-

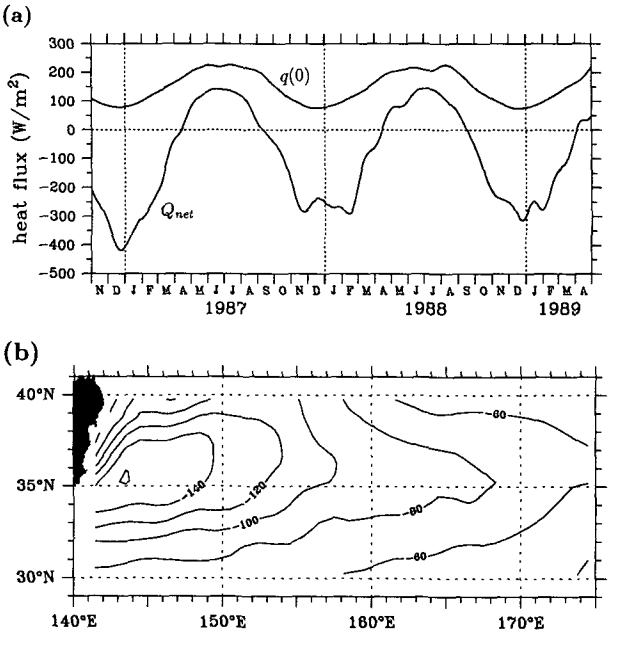

FIG. 3. (a) Time series of the net surface heat flux Q_{net} and the shortwave radiative flux $q(0)$ averaged in the model basin for the period of the Geosat ERM. (b) Horizontal pattern of the net surface heat flux averaged in 1987 and 1988 (units are W m^{-2}).

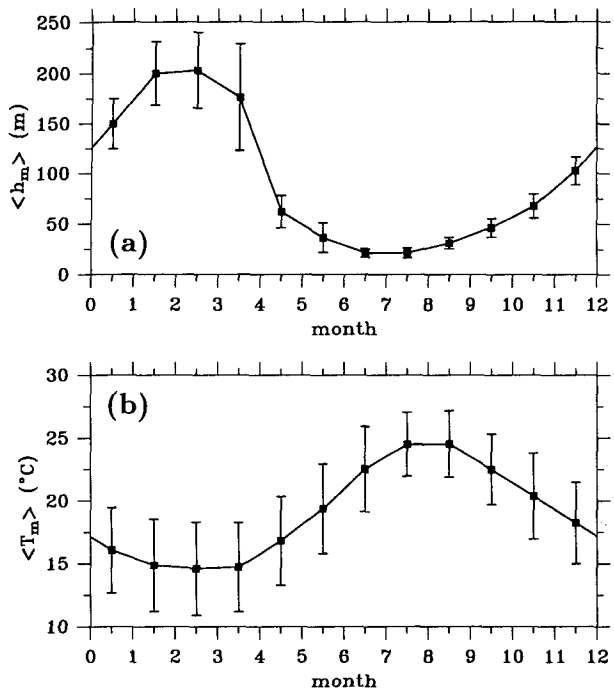

FIG. 4. Mixed-layer depth (h_m) and temperature (T_m) calculated according to Eq. (3) using the Levitus monthly mean climatology of the water temperature. Values have been averaged in the region of the model basin (see Fig. 1) and vertical bars denote the standard deviation.

roshio Extension. While the leapfrog scheme is used in time differencing, the implicit backward scheme (Matsuno 1966) is also adopted to suppress time-splitting instability (the daily surface data are kept the same for the four time steps in each day).

Levitus' (1982) monthly mean climatology is used for the model's initial condition. Based on the definition of (3), the mixed-layer temperature and depth are calculated using the monthly mean 1° × 1° temperature data of Levitus. The climatological T_m and h_m values averaged in the model basin are shown in Fig. 4. We started the numerical integration from 1 October 1986 with the T_m and h_m distributions of the September climatology. For the first 1.5 months of the calculation, we stepped forward in time using the contemporaneous ECMWF data, but keeping the surface height data fixed to the initial date of the Geosat ERM 15 November 1986. This "spinup" calculation adjusts the initial fields of T_m and h_m to the initial velocity field of the Kuroshio Extension. Experiments using the T_m and h_m data from a one-year model integration as the initial conditions were also tried. Both calculations yielded essentially the same results, suggesting the model predictions are not very sensitive to the chosen initial conditions.

For the boundary conditions of the model, we used data from both in situ observations and from the climatology. The Kuroshio enters the model basin south of the Japan coast, where the mixed-layer temperature and depth can vary substantially in time and space due to the path fluctuations of the Kuroshio (Hanawa and Hoshino 1988). To capture these fluctuations at the inflow to the Kuroshio Extension, we calculated the T_m and h_m values from CTD and XBT observations made near the Izu Ridge by various Japanese government agencies (see dashed line in Fig. 1). Figure 5 gives an example of the observed T_m and h_m values averaged for the grid of 34.0°–34.5°N (solid marks). To interpolate these observed data in time for the model calculation, we fit the data in six-month segments to a curve with annual and semiannual harmonics. The phases of these harmonics are determined from the climatological data shown in Fig. 4. While it fixes the phases of T_m and h_m, this method retains the amplitude changes of the inflow T_m and h_m as shown by the solid lines in Fig. 5. Along the other boundaries of the model basin where no in situ measurements were available, we used the monthly mean climatological data. Since no strong inflows exist along these boundaries, we expect the influence of using the climatological data on the model's interior to be small.

Due to the measurement scheme of the Geosat altimeter (repeat cycle of 17 days and subtrack separation of about 100 km), we confine ourselves in this study to the upper-ocean changes with time scales longer than weeks and spatial scales larger than 1° in longitude and 0.5° in latitude. Thermal structure changes owing to processes smaller than these scales are parameterized in the model dynamics by the subgrid-scale eddy diffusivity (A_h). Based on extensive SOFAR float obser-

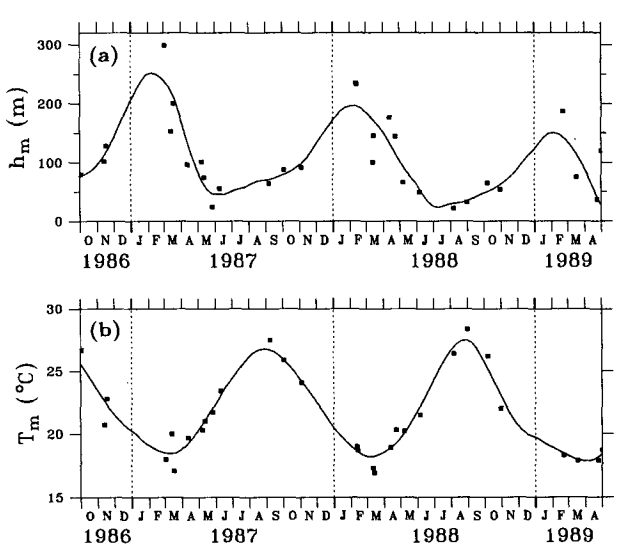

FIG. 5. Time series of h_m and T_m for the inflow grid between 34.0° and 34.5°N. Solid marks are values derived from the available CTD and XBT observations (based on *Data Report of KER, Phase II, No. 1–3*, published by Japan Oceanographic Data Center). Solid lines are the least-squares fits of the observed data, in which the phases of the annual and semiannual harmonics are fixed by the Levitus climatology (Fig. 4).

vations in the western North Atlantic, Rossby et al. (1983) showed that the eddy diffusivity calculated from float trajectories is nearly linearly related to the eddy kinetic energy (EKE) level. For the EKE level of 0.1 $m^2 s^{-2}$, a typical value for the surface Kuroshio Extension, their result suggested an eddy diffusivity in the order of 8×10^3 $m^2 s^{-1}$. In the following model calculations, this A_h value is used.

4. Model results

The model integration covers the time period from October 1986 to April 1989. Since the first 1.5 months of the calculation were used to adjust the climatological h_m and T_m fields to the observed initial velocity field, we focus in the following analyses on the results after 15 November 1986 when all input meteorological and surface height data are available. Figure 6 shows the time series of the modeled h_m and T_m variations averaged in the model basin (denoted below by $\langle h_m \rangle$ and $\langle T_m \rangle$). Both of the time series have well-defined annual cycles. The mixed-layer depths are shallowest, about 20 m, in summer and deepen steadily in the subsequent months until the following March. Accompanying the mixed-layer deepening, there is a gradual increase in the standard deviation of h_m. In April a sharp decrease in $\langle h_m \rangle$ occurs due to the change in the net surface heat flux from cooling to warming (see Fig. 3). The standard deviation of h_m in this month also reaches its maximum. These modeled phase changes in $\langle h_m \rangle$ and its standard deviation agree well with those of the Levitus climatology (Fig. 4a).

Apart from the dominant annual cycle, interannual changes are also apparent in the mixed-layer depth time series. The maximum $\langle h_m \rangle$ value, for example, varied from 275 m in 1987 to 240 m in 1989. Moreover, the deep winter mixed layer shoaled earlier in April of 1989 than in April of previous years. To look at these changes more closely, we plot in Fig. 7a the TKE balance of Eq. (10) averaged in the model basin. Notice that the maximum h_m value in early spring is essentially determined by the time integral of the entrainment velocity (w_e) from the fall of the previous year. As shown in Figs. 2 and 3, the amplitudes of the wind stress and

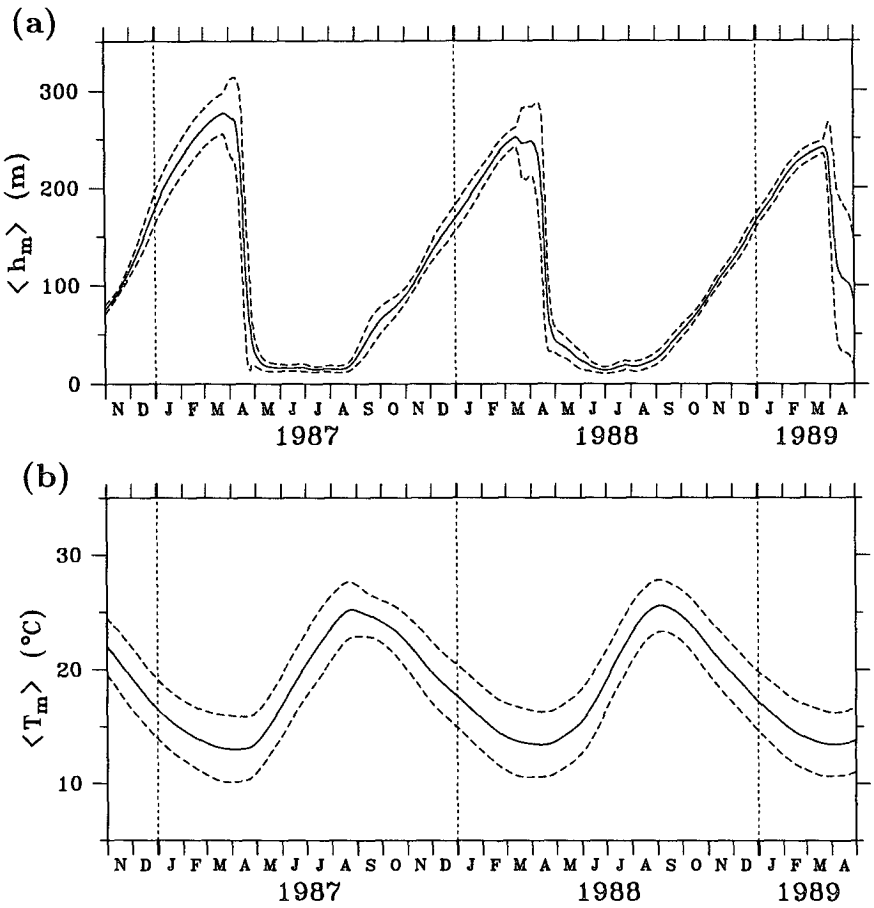

FIG. 6. Modeled mixed-layer depth (a) and temperature (b) changes during the Geosat ERM period. Solid lines are values averaged in the model basin and dashed lines denote their standard deviations.

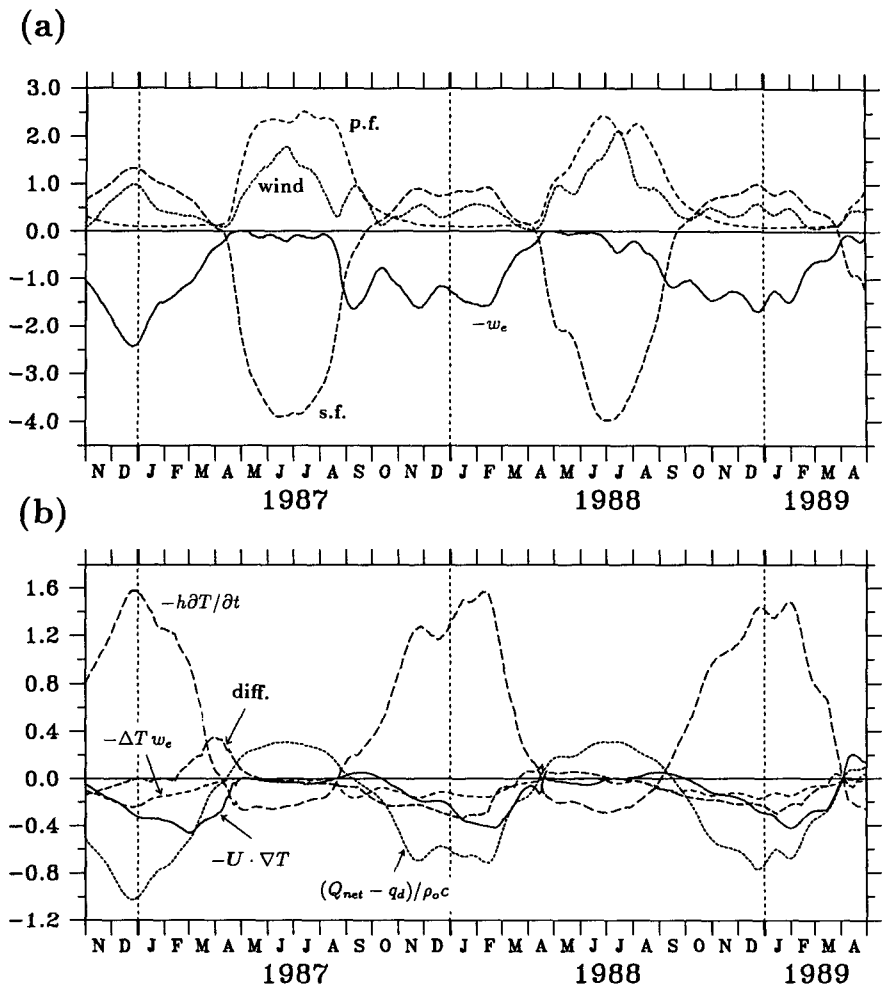

FIG. 7. (a) Basin-averaged balances of the terms contributing to the entrainment velocity w_e (see Eq. 10): "wind" denotes the wind stirring term $2m_0u_*^3/\alpha g h_m \Delta T$, "s.f." denotes the surface buoyancy term $-(Q_{net}+q_d)/\rho_0 c\Delta T - m_c(|Q_{net}| - Q_{net})/2\rho_0 c\Delta T$, and "p.f." denotes the radiation penetration term $2\int_{-h_m}^{0} q(z)dz/\rho_0 c h_m \Delta T$, respectively. The ordinate unit is 10^{-5} m s^{-1}). (b) Basin-averaged balances of the terms contributing to the mixed-layer heat content equation (Eq. 9). In the figure, "diff." denotes the horizontal eddy diffusion term $A_h(h_m\nabla^2 T_m - \Delta T \nabla^2 h_m)$. The ordinate unit is 10^{-4} m °C s^{-1}.

the net surface heat flux in the Kuroshio Extension region were greatly reduced in fall 1988–winter 1989 as compared to fall 1986–winter 1987 when the equatorial Pacific was in the warm phase of the El Niño–Southern Oscillation (Qiu and Joyce 1992). In the TKE balance (Fig. 7a), both effects of the weak wind stirring and the weak surface cooling in fall 1988–winter 1989 attenuated the entrainment, contributing to the weaker maximum of $\langle h_m \rangle$ in the early spring of 1989. Also, the earlier sign reversal in the net heat flux in April of 1989 (Fig. 3a) was responsible for the earlier erosion of the deep mixed layer as we noted in Fig. 6a. Due to these interannual changes of $\langle h_m \rangle$ in amplitude and in phase, it is reasonable to expect that the climatological $\langle h_m \rangle$ in March (200 m; Fig. 4a) is shallower than the modeled $\langle h_m \rangle$ values.

The modeled $\langle T_m \rangle$ variations also seem to agree well with the Levitus climatology. Both Figs. 4b and 6b show minima of $\langle T_m \rangle$ in March/April and maxima in August/September and both indicate that the standard deviation of T_m is larger in spring than in fall. Interannual changes in the $\langle T_m \rangle$ time series are not very obvious, despite the fact that the entrainment was reduced in the two post-ENSO years. Examining the term balance for the mixed-layer temperature change [Eq. (9), Fig. 7b] reveals that the temporal changes of $\langle T_m \rangle$ are more sensitive to terms such as the surface heat flux input and the horizontal advection than to the cold water entrainment through the bottom of the mixed layer. The minimum $\langle T_m \rangle$ value in Fig. 6b, however, is slightly different in the three years (13.0°C in 1987, 13.4°C in 1988, and 13.2°C in 1989); but

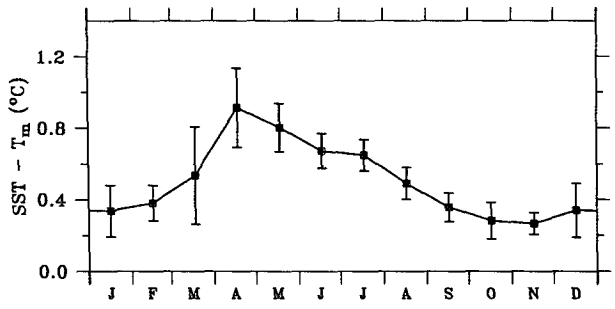

FIG. 8. Differences between the SST and the mixed-layer temperature calculated using the Levitus monthly mean climatology of the water temperature. Values have been averaged in the region of the model basin and vertical bars denote the standard deviation.

this difference seems to be primarily due to the interannual changes in Q_{net} (see Fig. 7b; notice that the integrated heat loss from the ocean to the atmosphere is minimum in fall 1987–winter 1988). The small interannual fluctuations in Fig. 6b seem to imply that the surface wind stress changes in the interannual frequency band are not effective in changing the mixed-layer temperature in the Kuroshio Extension region.

A more stringent check on the model performance is to compare horizontal patterns of T_m with available in situ observations. By compiling ships, buoys, and other observational sources, the Japan Meteorological Agency has published the monthly mean SST maps of the western North Pacific for the past decade. Although the SST is not equal to the mixed-layer temperature (see Fig. 8), the horizontal patterns of the SST, nevertheless, can be regarded as good indicators for the modeled horizontal patterns of T_m. Figure 9 shows the maps of the monthly mean SSTs and the monthly mean mixed-layer temperatures from the model. Comparisons between the two results show that the model calculation captured most fluctuations of the Kuroshio Extension's two quasi-stationary meanders (centered near 143° and 149°E). For example, the second meander of the Kuroshio Extension is not as well developed in December 1986 as in June 1987, the two meanders weaken in December 1987 and coalesce as one large meander in June 1988, and in December 1988 the second meander reappears in an unusual location downstream of 151°E. The model calculation also reproduced the permanent southward deflection of the Kuroshio Extension near 157°E and predicted sporadic isotherm distortions due to, for example, warm water intrusions near (38°N, 148°E) in December 1986, near (39°N, 150°E) and (38°N, 160°E) in December 1987, and a cold water intrusion near (33°N, 148°E) in June 1988.

There are discrepancies between the observations and the model predictions. The T_m values in the model's northwestern corner are in general not as cold in the winter months as the SSTs. This is largely due to the fact that, unlike the Kuroshio inflow south of Japan, we were not able to specify the cold Oyashio inflow in this region from in situ observational data. Due to limitations in the model's temporal and spatial resolution, some of the modeled meanders and warm water intrusions in Fig. 9a appear less sharp than in the SST maps. Also, the T_m gradients in the downstream region of the model basin in June 1988 are rather different from the corresponding SST map. Despite these discrepancies we believe that the present model is adequate in hindcasting the major thermal changes of the upper ocean and can be used to help clarify the roles played by the Kuroshio Extension in influencing the upper-ocean heat balance.

5. Influence of the Kuroshio Extension on the upper-ocean heat balance

To understand the Kuroshio Extension's contribution to the upper-ocean heat balance, it is instructive to know how neglecting horizontal advection in the model can alter the upper-ocean thermal structure. To do so, we reran the model under the same conditions as for Fig. 9a, except for setting $\mathbf{U}_m = 0$ in Eqs. (8) and (9). As shown in Fig. 10a, the resultant T_m patterns in this case become more or less zonally oriented because the surface heat flux, which has a strong latitudinal dependency, is now the dominant term in determining the mixed-layer temperature changes (see Fig. 7b). Compared to their corresponding maps in Fig. 9a, the isotherms in Fig. 10a captured no zonal fluctuations associated with the meandering Kuroshio Extension. Notice that the influence of the Kuroshio Extension is not confined to the energetic current region between 33° and 37°N; the differences in T_m between the two model results (Fig. 10b) reveal that the horizontal advection essentially has influence over the entire region of the model basin. Also notice that inclusion of the horizontal advection only raises the mixed-layer temperature in the upstream Kuroshio Extension region west of 150°E. Over the vast downstream region, the advective effect is to lower the mixed-layer temperature.

To quantitatively discuss the role of the current advection in determining the upper-ocean thermal structures, it is helpful to rewrite the temperature conservation equation (9) as follows:

$$\frac{\partial T_m}{\partial t} = -(\mathbf{u}_g + \mathbf{u}_e)\cdot\nabla T_m + \frac{Q_{\text{net}} - q_d}{\rho_0 c h_m} - \frac{\Delta T w_e}{h_m} + A_h\left(\nabla^2 T_m - \frac{\Delta T}{h_m}\nabla^2 h_m\right). \quad (14)$$

Anticipating that the Ekman and the geostrophic flows ($\mathbf{u}_e$ and $\mathbf{u}_g$) contribute disparately to the mixed-layer temperature changes, we have separated the advection term into the Ekman and the geostrophic components in Eq. (14). In Fig. 11, we plot the zonally averaged term balances of Eq. (14) as a function of time and

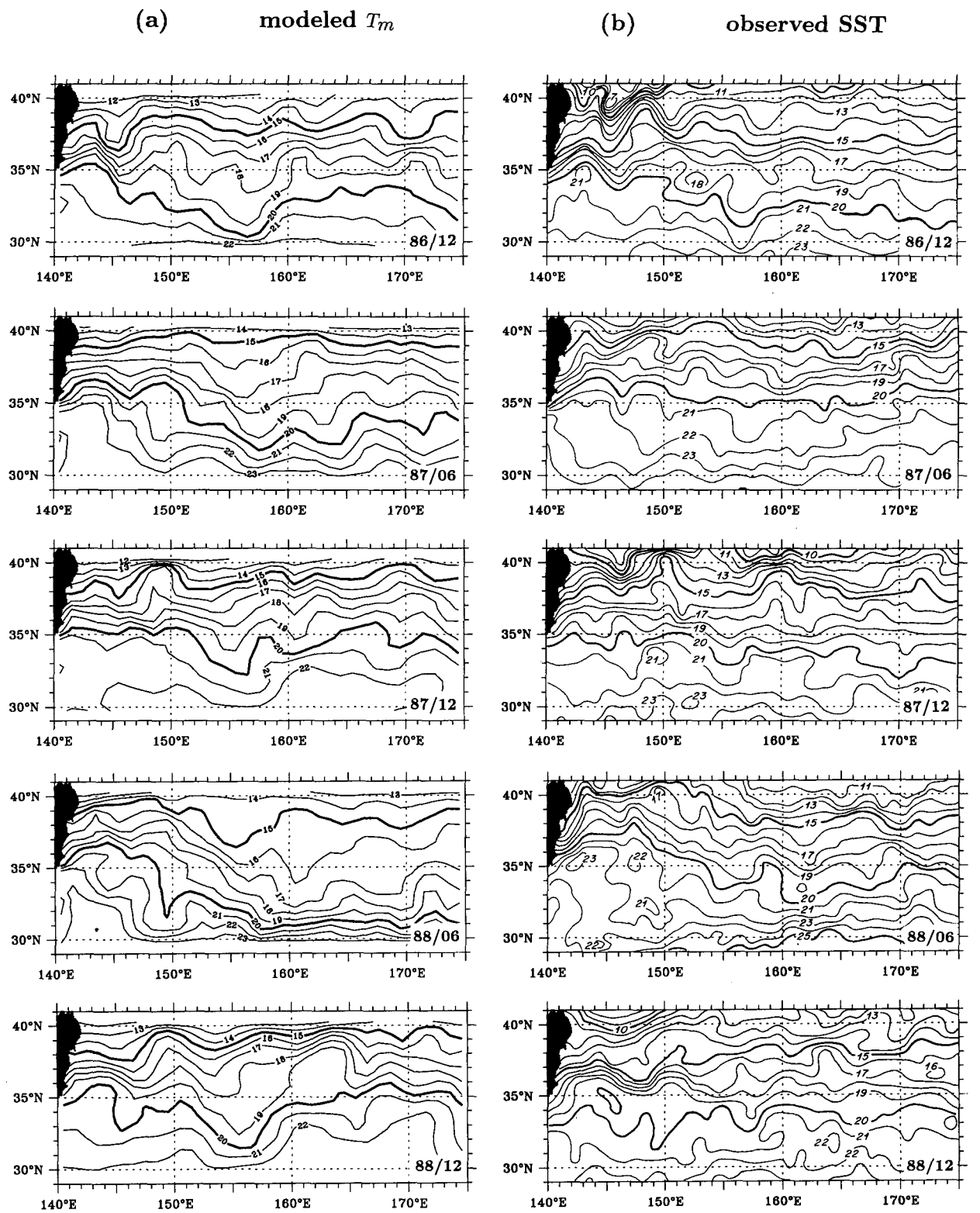

FIG. 9. (a) Modeled monthly mean mixed-layer temperature distributions (contour units are °C). Year/month is indicated in the lower right-hand corner of each map. (b) Monthly mean sea surface temperature distributions (based on *The Ten-Day Marine Report, No. 1446–1520,* published by Japan Meteorological Agency).

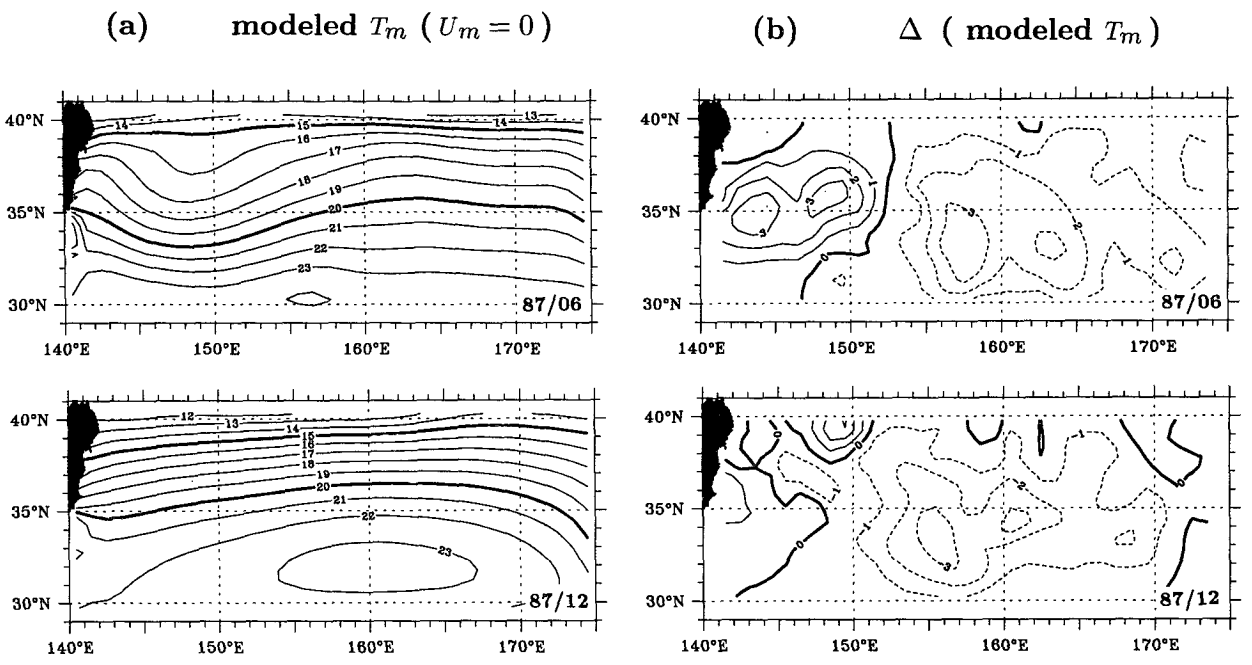

FIG. 10. (a) Monthly mean mixed-layer temperature distributions derived from the model neglecting the horizontal advections. (b) Differences in T_m between the model result with horizontal advections (Fig. 9a) and that without (Fig. 10a). Positive (negative) values indicate T_m in the advective model is warmer (colder) than that in the nonadvective model. Contour units are °C.

latitude. The temperature tendency term $\partial T_m/\partial t$ bears a pattern very similar to the surface thermal forcing term $(Q_{\text{net}} - q_d)/\rho_0 c h_m$ (Figs. 11a and 11b). The fact that the surface thermal forcing controls the gross seasonal cycle of the upper-ocean water temperature is not surprising, since the Kuroshio Extension *is* one of the regions where the surface thermal forcing is strongest. A more careful check, however, reveals that the surface thermal forcing dominates the T_m changes only in the period from April to July when the deep winter mixed layer erodes and before the deepening of the renewed mixed layer. As summarized in Table 1, the surface thermal forcing in the months from August to March only accounts for about 50% of the mixed-layer temperature changes. From Table 1 also notice that the annually integrated contribution of the surface thermal forcing to T_m is *positive,* that is, the atmosphere warms the mixed layer. This is somewhat counterintuitive because the annually integrated net surface heat flux in this region is negative (Fig. 3b), that is, the ocean is losing heat to the atmosphere. This apparent paradox arises due to the changes in the mixed-layer depth: though large in magnitude, the heat loss in winter occurs in a deep mixed layer (~200 m) due to the convective overturning, whereas the small heat input in summer is trapped above a shallow seasonal thermocline (~20 m).

The warming effect on T_m by the surface thermal forcing is nearly counterbalanced by the other terms in Eq. (14). (A perfect annual equilibrium of T_m would require the integrated $\partial T_m/\partial t$ value to be zero; it is not exactly zero in Table 1 because of the interannual changes in T_m associated with the ENSO event as we discussed in the last section.) The vertical entrainment term $-\Delta T w_e/h_m$ always works to lower T_m (Fig. 11c). Table 1 shows that this term, when annually integrated, offsets 35% of the warming effect due to the surface thermal forcing. Clearly, the surface thermal forcing and the vertical turbulent mixing alone (in other words, the vertical, one-dimensional processes alone) cannot maintain the annual equilibrium of the mixed-layer temperature in the Kuroshio Extension region. Horizontally, the surface wind over the Kuroshio Extension generally blows eastward (Fig. 2b), and this induces southward Ekman transport, resulting in temperature flux divergence ($-\mathbf{u}_e \cdot \nabla T_m < 0$). An exception is during the summertime when the surface wind direction reverses, which causes a convergent temperature flux in the upper ocean (see Fig. 11d). The annually integrated effect of the Ekman transport contributes, as shown in Table 1, an offset of 16.5% to the warming effect due to the surface thermal forcing.

Unlike the previous four terms in Eq. (14) that all have well-defined meridionally coherent patterns, the temperature advection associated with the geostrophic flows is less coherent (Fig. 11e). This is so because of the large-amplitude meanders and pinched-off eddies in the Kuroshio Extension region, which cause the inner product of $\mathbf{u}_g$ and ∇T_m to be a complicated function of time and space. There are, nevertheless, places where the temperature advection has a stable sign. For example, in areas north of the mainstream Kuroshio Ex-

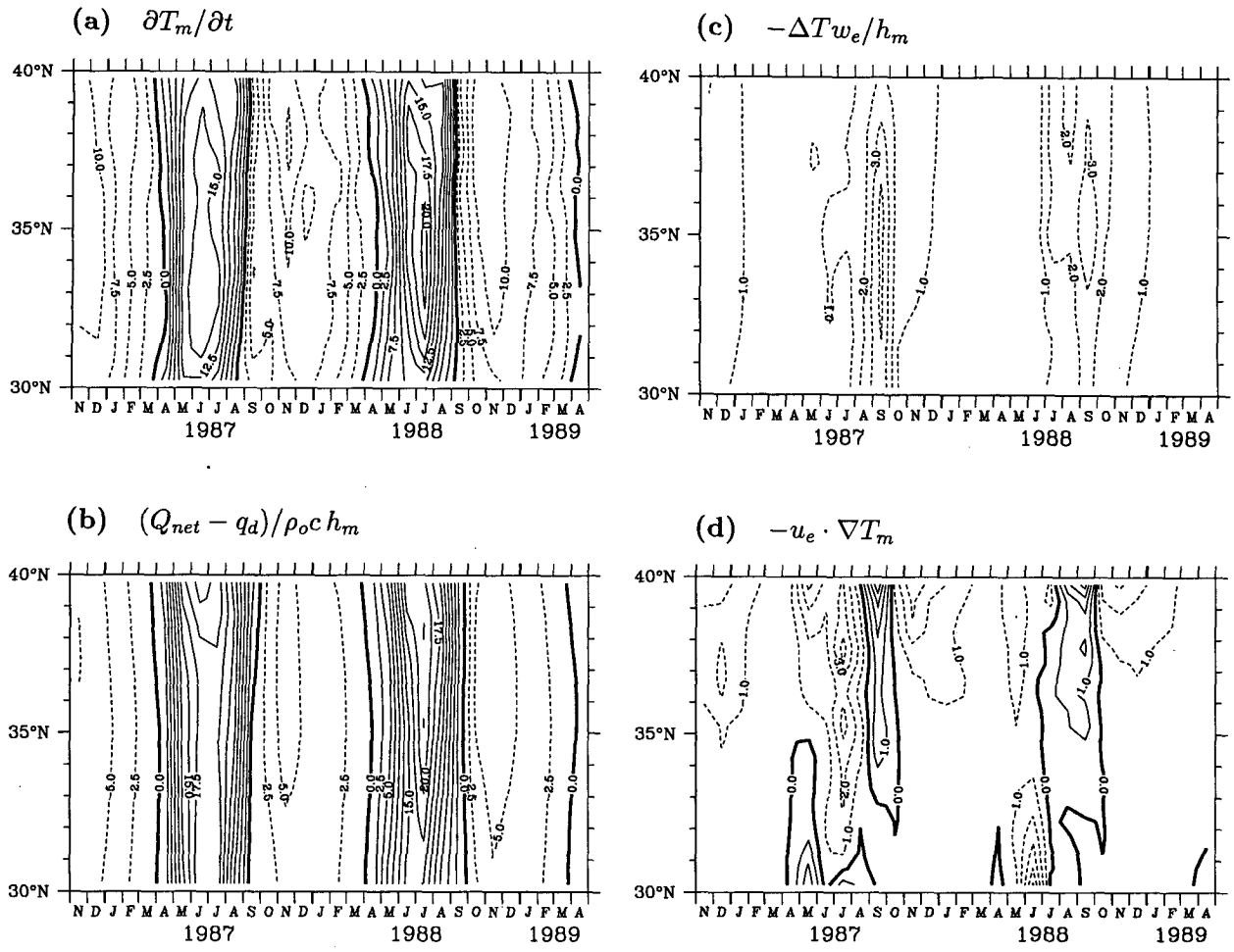

FIG. 11. Zonally averaged balances of the terms in the mixed-layer temperature equation (14) plotted as a function of time. All values have units of 10^{-7} °C s^{-1}. Notice that the contour intervals in (a), (b), (e), and (f) are 2.5 and those in (c) and (d) are 1.0.

tension (latitude > 37.5°N), $-\mathbf{u}_g \cdot \nabla T_m$ is in general positive, a result reflecting the northward heat transfer due to the frequent shedding of warm-core eddies (e.g., Yasuda et al. 1992). In areas south of the Kuroshio Extension (latitude < 34°N), on the other hand, the $-\mathbf{u}_g \cdot \nabla T_m$ term is mostly negative, due to the fact that a persistent southward flow associated with the southern recirculation gyre exists in the area east of 148°E (Fig. 1), and the meridional temperature gradient in this area is always negative due to the meridionally differential surface heating/cooling. Notice that during the summertime the zonally averaged value of $-\mathbf{u}_g \cdot \nabla T_m$ south of the Kuroshio Extension is positive (see Fig. 11e). The sign changes because the meridional temperature gradient in the recirculation gyre region is weakest during the summer (Fig. 12) and this reduces the magnitude of the meridional temperature flux $-v_g \partial T_m/\partial y$, which, in other months of the year, is the dominant component in $-\mathbf{u}_g \cdot \nabla T_m$. The weak surface temperature gradient in August and September is associated with the weak gradient in the air–sea net heat flux in these months. The weakening of the summertime meridional temperature gradient in the recirculation gyre region seems to have a significant influence on the basin-averaged $-\mathbf{u}_g \cdot \nabla T_m$ values. Table 1 shows that the geostrophic advection term has positive values in August and September, contrasted with the negative values during the rest of the year.

The temperature advection due to the geostrophic flows also has a strong zonal dependence: in the region west of 150°E, $-\mathbf{u}_g \cdot \nabla T_m$ is always positive, suggesting that the warm water inflow increases the mixed-layer temperature in the upstream Kuroshio Extension. In the downstream region of 150°E, as we have found previously, $-\mathbf{u}_g \cdot \nabla T_m$ is mostly negative due to the presence of the southward recirculating flows. Together with the southward Ekman flows, the advection in the downstream Kuroshio Extension works to decrease the mixed-layer temperature. This zonal dependence, in fact, explains what we saw in Fig. 10b: that T_m would be colder (warmer) in the upstream (downstream) Kuroshio Extension were no horizontal advection in-

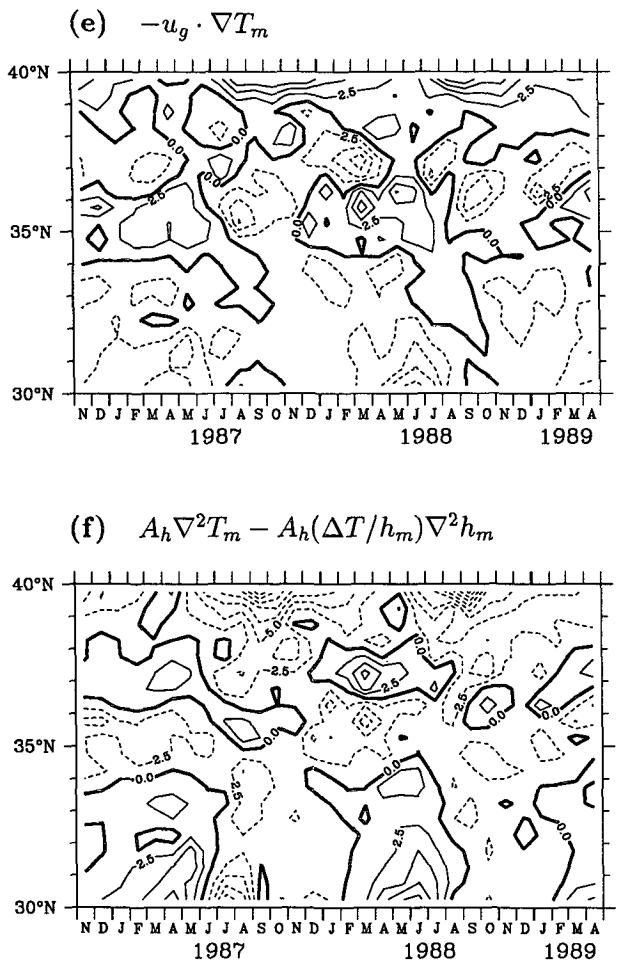

FIG. 11. (*Continued*)

cluded in the model calculation. Although the geostrophic advection is important to the local temperature balances, its effect, when integrated spatially and annually, is not large and offsets about 12% of the warming effect of the surface thermal forcing. Finally, Fig. 11f shows the local fluctuations of the $-\mathbf{u}_g \cdot \nabla T_m$ term are partially balanced by the horizontal eddy diffusion term. This suggests that the horizontal eddy diffusion is effective in removing the T_m anomalies caused by the geostrophic flows locally crossing the isotherms. Because of the large temperature gradient and the high eddy variability in the boundary current extension region, the horizontal eddy diffusion makes a substantial contribution to the upper-ocean temperature budget: when annually averaged, it is comparable to the effect caused by the cold water entrainment through the base of the mixed layer and offsets the remaining 35% of the warming effect due to the surface thermal forcing (Table 1).

6. Conclusions

Western boundary current extension regions, such as the Kuroshio after separation from the Japan coast, and the Gulf Stream downstream of Cape Hatteras, are where intensive air–sea interactions take place. Although it is conceivable that the presence of the boundary current jets and their energetic fluctuations can play a substantial role in influencing the upper-ocean heat balances, their exact role has not been well understood because of the lack of continuous surface velocity information over a large horizontal extent. The advent of satellite altimetric observations has made it feasible now to estimate the geostrophic component of the surface velocities with temporal repetition and global coverage. In the present study we combined the sea surface height data of the Geosat altimeter ERM with a two-dimensional mixed-layer model and investigated the upper-ocean heat balance and the role of current advection in the Kuroshio Extension region (30°–40°N, 141°–175°E).

TABLE 1. Monthly balances of the terms contributing to the mixed-layer temperature change [see Eq. (14)]. Values have been averaged in the model basin and over the time period of the Geosat ERM (December 1986–April 1989). Units are 10^{-7} °C s^{-1}.

	$\frac{\partial T_m}{\partial t}$	$-\mathbf{u}_e \cdot \nabla T_m$	$-\mathbf{u}_g \cdot \nabla T_m$	$\frac{Q_{net} - q_d}{\rho_0 c h_m}$	$\frac{-w_e \Delta T}{h_m}$	Horizontal eddy diffusion
Jan	−7.46	−0.83	−0.87	−3.80	−0.81	−1.14
Feb	−5.50	−0.62	−0.99	−2.70	−0.56	−0.63
Mar	−2.17	−0.30	−0.70	−1.07	−0.25	0.15
Apr	1.41	−0.29	−0.25	1.30	−0.07	0.72
May	10.11	−0.92	−0.16	10.17	−0.30	1.32
Jun	16.15	−1.20	−0.53	18.46	−0.63	0.05
Jul	14.95	−1.14	−0.27	19.54	−1.43	−1.73
Aug	6.62	0.37	0.07	11.42	−2.10	−3.14
Sept	−5.06	0.96	0.10	0.32	−3.29	−3.15
Oct	−8.94	−0.44	−0.13	−4.05	−1.55	−2.77
Nov	−10.38	−0.94	−0.41	−5.69	−1.33	−2.01
Dec	−9.15	−1.03	−0.46	−5.23	−1.15	−2.01
Annually integrated	0.57	−6.38	−4.61	38.67	−13.48	−13.62

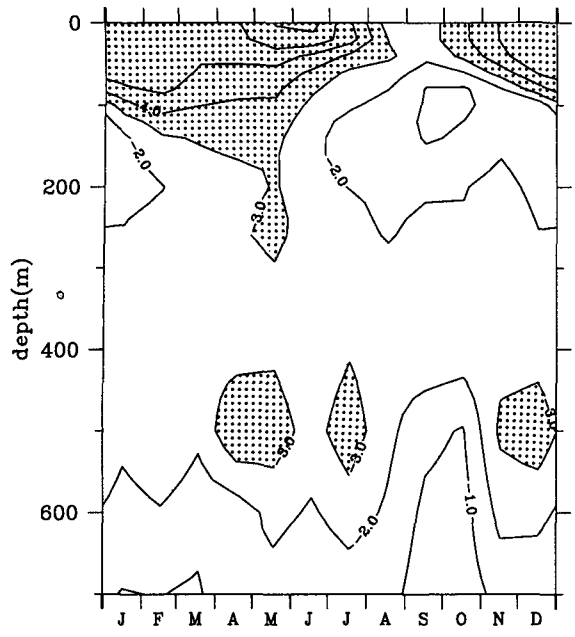

FIG. 12. Meridional temperature gradient $\partial T/\partial y$ averaged in the southern recirculation gyre portion of the model basin (29.5°–32.5°N, 148.5°–175.5°E, see Fig. 1). All values have unit of 10^{-6} °C m^{-1} and are calculated from the Levitus monthly mean climatology. Areas where $|\partial T/\partial y| > 3.0 \times 10^{-6}$ °C m^{-1} are stippled.

The mixed-layer model we used was based on the thermodynamics of the upper ocean, which includes both horizontal advective and diffusive effects. For the horizontal advection, both the geostrophic and the Ekman components were taken into account. The vertical entrainment through the base of the mixed layer was determined by the turbulent kinetic energy balance proposed by Davis et al. (1981), with the coefficient for the vertical wind mixing chosen to be $m_0 = 0.5$. Although m_0 is an empirical parameter in the model formulation, we point out that the entrainment velocity and the temporal evolution of the mixed-layer temperature are so strongly constrained by the surface buoyancy forcing over the Kuroshio Extension (see Fig. 7) that choosing a different m_0 value (say, 0.4–0.6) essentially produces results similar to those shown in the previous two sections.

Using the sea surface height data determined previously by Qiu et al. (1991) and the surface wind and heat flux data from the ECMWF, we hindcast the temporal evolution of the mixed-layer depth (h_m) and temperature (T_m) in the Kuroshio Extension region from November 1986 to April 1989. The seasonal cycle of the basin-averaged T_m and h_m agreed closely both in phase and in amplitude with that from the Levitus climatology. Deviations from the climatology are found to be sensitive to the interannual fluctuations in the surface wind and thermal forcing: when the surface wind and cooling were relatively strong during the 1986–1987 ENSO event, the mixed layer in the Kuroshio Extension was deeper and the erosion of the winter mixed layer was later in time as compared to the two post-ENSO years. Comparing the horizontal patterns of the modeled T_m with available monthly mean SST observations further showed that the model was able to capture most features of temperature fluctuations with horizontal scales greater than 200 km.

Like in the Gulf Stream region beyond Cape Hatteras, the annually averaged net heat flux from the atmosphere to the ocean over the Kuroshio Extension is negative. This, however, does not imply that the annually integrated effect of the surface thermal forcing is to lower the T_m. In fact, since the surface buoyancy forcing is proportional to the heat content ($\sim h_m T_m$) changes, its annually integrated effect is to increase the mixed-layer temperature, because the mixed layer is much deeper during the cooling phase than during the warming phase. The warming effect of the surface thermal forcing is partially counterbalanced by the vertical turbulent entrainment (35% when annually integrated), but the remaining 63% is offset by horizontal processes. Due to the persistent westerlies over the Kuroshio Extension, the Ekman transport is in general southward (except for August and September), which results in the temperature flux divergence and a decrease in the mixed-layer temperature. The advection due to the geostrophic flows, on the other hand, has a strong zonal dependence: the warming effect of the inflow Kuroshio is confined to the upstream Kuroshio Extension. In the downstream region east of 150°E, temperature fluxes transported southward by the recirculation gyre and eastward by the North Pacific Current exceed the temperature influxes. This temperature flux divergence decreases the mixed-layer temperature in the downstream Kuroshio Extension. An exception is during the summertime when the meridional T_m gradient weakens, and the temperature flux divergence diminishes. Although the effect of the geostrophic advection is relatively small when integrated in space and time, it is usually the dominant term in the local upper-ocean heat balance. The horizontal eddy diffusion is found to be effective in reducing the local extrema of T_m induced by the geostrophic advection.

In conclusion, we note that the temperature balance presented above holds true only for the surface mixed layer in the Kuroshio Extension region. Below this surface layer, the temperature balance is likely to be different. For example, the Ekman advection is extinguished, and the vertical eddy diffusion has to be parameterized differently than in Eq. (7). Although Table 1 shows that the effect of the geostrophic advection, when integrated annually in the model basin, is to lower the mixed-layer temperature, our previous discussion suggested that this is largely due to the strong, negative temperature gradient $\partial T_m/\partial y$ in the recirculation gyre. When the magnitude of $\partial T_m/\partial y$ decreases, say, smaller than 3×10^{-6} °C m^{-1} as in August and September

(Fig. 12), the basin-averaged $-\mathbf{u}_g \cdot \nabla T_m$ can be positive (Table 1). Since the magnitude of the meridional temperature gradient in the recirculation gyre is always less than this critical value at depths greater than 100 m (Fig. 12), it is reasonable to expect the geostrophic advection to have an effect opposite to that in the surface mixed layer (i.e., to increase the water temperature). Clearly, the present model is too simple to provide a quantitative argument on the heat balance below the mixed layer. Since the heat balance below the mixed layer is an important component if we are to understand the overall heat budget in the boundary current extension regions, future studies involving more observational data and a more sophisticated ocean model are required.

Acknowledgments. James Price carefully read the manuscript and made many helpful suggestions. We are also grateful to Terrence Joyce, Hsiao-Ming Hsu, Steven Lentz, Albert Plueddemann, and the two reviewers for their critical comments. The ECMWF wind and heat flux data were provided by the National Center for Atmospheric Research. We appreciate the technical support from Michael Caruso, Janet Fredricks, and Toshiko Turner. This study was supported by the Office of Naval Research under Grant N00014-92-J-1656 and by the National Oceanic and Atmospheric Administration under Grant NA16RC0468-01.

REFERENCES

Barnier, B., and J.-Y. Simonot, 1990: Net surface heat flux over the North and South Atlantic in 1985–1986 from day 1 predictions of the European Centre for Medium-Range Weather Forecasts. *J. Geophys. Res.*, **95,** 13 301–13 311.

Bingham, F. M., 1992: Formation and spreading of subtropical mode water in the North Pacific. *J. Geophys. Res.*, **97,** 11 177–11 189.

Bryden, H. L., and E. C. Brady, 1985: Diagnostic model of the three dimensional circulation in the upper equatorial Pacific Ocean. *J. Phys. Oceanogr.*, **15,** 1255–1273.

Davis, R. E., R. de Szoeke, and P. Niiler, 1981: Variability in the upper ocean during MILE. Part II: Modeling the mixed layer response. *Deep-Sea Res.*, **28,** 1453–1475.

Deardorff, J. W., G. E. Willis, and D. K. Lilly, 1969: Laboratory investigation of non-steady penetrative convection. *J. Fluid Mech.*, **35,** 7–35.

Denman, K. L., 1973: A time-dependent model of the upper ocean. *J. Phys. Oceanogr.*, **3,** 173–184.

——, and M. Miyake, 1973: Upper layer modification at Ocean Station *Papa:* Observations and simulation. *J. Phys. Oceanogr.*, **3,** 185–196.

de Ruijter, W. P. M., 1983: Effects of velocity shear in advective mixed-layer models. *J. Phys. Oceanogr.*, **13,** 1589–1599.

Enfield, D. B., 1986: Zonal and seasonal variations of the near-surface heat balance of the equatorial Pacific Ocean. *J. Phys. Oceanogr.*, **16,** 1037–1054.

Garwood, R. W., Jr., 1977: An oceanic mixed-layer model capable of simulating cyclic states. *J. Phys. Oceanogr.*, **7,** 455–471.

Hanawa, K., 1987: Interannual variations of the winter-time outcrop area of subtropical mode water in the western North Pacific Ocean. *Atmos.-Ocean,* **25,** 358–374.

——, and I. Hoshino, 1988: Temperature structure and mixed layer in the Kuroshio region over the Izu Ridge. *J. Mar. Sci.*, **46,** 683–700.

Hsiung, J., 1985: Estimates of global oceanic meridional heat transport. *J. Phys. Oceanogr.*, **15,** 1405–1413.

Isemer, H.-J., and L. Hasse, 1987: *The Bunker Climate Atlas of the North Atlantic Ocean.* Vol. 2, *Air–Sea Interactions.* Springer-Verlag, 252 pp.

Jerlov, N. G., 1968: *Optical Oceanography.* Elsevier, 194 pp.

Kelly, K. A., and S. T. Gille, 1990: Gulf Stream surface transport and statistics at 69°W from the Geosat altimeter. *J. Geophys. Res.*, **95,** 3149–3161.

Kraus, E. B., and J. S. Turner, 1967: A one-dimensional model of the seasonal thermocline: II. The general theory and its consequences. *Tellus,* **19,** 98–106.

Lamb, P. J., 1984: On the mixed-layer climatology of the north and topical Atlantic. *Tellus,* **36A,** 292–305.

Levitus, S., 1982: Climatological atlas of the world ocean. NOAA Prof. Paper No. 13, U.S. Govt. Printing Office, Washington, DC, 173 pp.

List, R. J., 1984: *Smithsonian Meteorological Tables.* Smithsonian Institution Press, 572 pp.

McPhaden, M. J., 1982: Variability in the central equatorial Indian Ocean. Part II: Oceanic heat and turbulent energy balances. *J. Mar. Res.*, **40,** 403–419.

Martin, P. J., 1985: Simulation of the mixed layer at OWS November and Papa with several models. *J. Geophys. Res.*, **90,** 903–916.

Masuzawa, J., 1972: Water characteristics of the North Pacific central region. *Kuroshio-Its Physical Aspects,* H. Stommel and K. Yoshida, Eds., University of Tokyo Press, 95–127.

Matsuno, T., 1966: Numerical integrations of the primitive equations by a simulated backward difference method. *Meteor. Mag.*, **44,** 76–84.

Niiler, P. P., 1975: Deepening of the wind-mixed layer. *J. Mar. Sci.*, **33,** 405–422.

——, and E. B. Kraus, 1977: One-dimensional models of the upper ocean. *Modelling and Prediction of the Upper Layers of the Ocean,* E. B. Kraus, Ed., Pergamon Press, 152–172.

Paduan, J. D., and R. A. de Szoeke, 1986: Heat and energy balances in the upper ocean at 50°N, 140°W during November 1980 (STREX). *J. Phys. Oceanogr.*, **16,** 25–38.

Paulson, C. A., and J. J. Simpson, 1977: Irradiative measurements in the upper ocean. *J. Phys. Oceanogr.*, **7,** 952–956.

Price, J. F., R. A. Weller, and R. Pinkel, 1986: Diurnal cycling: Observations and models of the upper ocean response to diurnal heating, cooling, and wind mixing. *J. Geophys. Res.*, **91,** 8411–8427.

Qiu, B., and T. M. Joyce, 1992: Interannual variability in the mid- and low-latitude western North Pacific. *J. Phys. Oceanogr.*, **22,** 1062–1079.

——, K. A. Kelly, and T. M. Joyce, 1991: Mean flow and variability in the Kuroshio Extension from Geosat altimetry data. *J. Geophys. Res.*, **96,** 18 491–18 507.

Rossby, H. T., S. C. Riser, and A. J. Mariano, 1983: The western North Atlantic—A Lagrangian viewpoint. *Eddies in Marine Science,* A. R. Robinson, Ed., Springer-Verlag, 66–91.

Stevenson, J. W., and P. P. Niiler, 1983: Upper ocean heat budget during the Hawaii-to-Tahiti shuttle experiment. *J. Phys. Oceanogr.*, **17,** 1984–1907.

Talley, L. D., 1984: Meridional heat transport in the Pacific Ocean. *J. Phys. Oceanogr.*, **14,** 231–241.

——, and M. E. Raymer, 1982: Eighteen degree water variability. *J. Mar. Res.*, **40,** 757–775.

Thompson, R. O. R. Y., 1976: Climatological numerical models of the surface mixed layer of the ocean. *J. Phys. Oceanogr.*, **6,** 496–503.

Trenberth, K. E., W. G. Large, and J. G. Olson, 1990: The mean annual cycle in global ocean wind stress. *J. Phys. Oceanogr.*, **20,** 1742–1760.

Worthington, L. V., 1976: On the North Atlantic circulation. *The Johns Hopkins Oceanographic Studies.* **6,** The Johns Hopkins University Press, 110 pp.

Yasuda, I., K. Okuda, and M. Hirai, 1992: Evolution of a Kuroshio warm-core ring—Variability of the hydrographic structure. *Deep-Sea Res.*, **39,** S131–S161.